Available online at www.sciencedirect.com

ScienceDirect

Advances in Space Research 65 (2020) 2391–2404

ADVANCES IN SPACE RESEARCH (a COSPAR publication)

www.elsevier.com/locate/asr

On the possible contribution of ionospheric vertical drifts to TEC modelling in low latitudes

Valence Habyarimana [a,*], John Bosco Habarulema [b,c], Patrick Mungufeni [a]

[a] Department of Physics, Mbarara University of Science and Technology, Mbarara, Uganda
[b] South African National Space Agency (SANSA) Space Science, 7200 Hermanus, South Africa
[c] Department of Physics and Electronics, Rhodes University, 6140 Makhanda, South Africa

Received 18 September 2019; received in revised form 1 February 2020; accepted 6 February 2020
Available online 17 February 2020

Abstract

A single station empirical total electron content (TEC) model based on the Global Navigation Satellite System (GNSS) data during 2001–2015 is presented over the African low latitude region. For the first time, we have investigated the contribution of ionospheric vertical drifts to TEC modelling by including vertical **E**×**B** drift generated from Communication/Navigation Outage and Forecasting System (C/NOFS) satellite data as an input along with diurnal variation, seasonal variation, solar activity and geomagnetic activity representations. The inputs were used to develop the neural network (NN) TEC model over Mbarara, MBAR (0.6°*S*, 30.74°*E*; 10.22°*S* geomagnetic) which was later validated on independent dataset that was selected from different solar activity periods. The model without vertical **E**×**B** drift as an input gave mean absolute error (MAE) of 4.013 TECU. Inclusion of the vertical **E**×**B** drift input reduced the MAE to 3.757 TECU equivalent to an average improvement of 6.4% in TEC modelling. The maximum improvement attained was around 13% during the high solar activity period. The correlation coefficient (R) values for models without and with vertical **E**×**B** drift input were 0.954 and 0.958 respectively. Our results show that availability of ionospheric vertical drift data has the potential of improving future TEC modelling in low latitude regions.
© 2020 COSPAR. Published by Elsevier Ltd. All rights reserved.

Keywords: Neural networks; Total electron content; Vertical **E**×**B** drift

1. Introduction

The equatorial ionosphere is dynamic due to the complex electrodynamic processes (Fejer, 1981, 2002; Heelis, 2004). Examples of electrodynamic processes are related to equatorial fountain effect, vertical coupling between the lower and upper atmosphere, pre-reversal enhancement and prompt penetration electric field (Burke et al., 1984; Abdu, 2001; Fejer, 2011; Astafyeva et al., 2018). These processes modify the ionosphere causing a great influence on the radio waves traversing through it and this may limit the performance and accuracy of transionospheric communication and navigation link systems (Hajra et al., 2016). Generally, the regions which lie within the equatorial ionization anomaly are more vulnerable to ionospheric effects such as group path delay, radio frequency carrier phase advance, Faraday polarization rotation, angular refraction, frequency doppler shift, and scintillation (Norsuzila, 2008). Each of the above mentioned effects is influenced by the electron density, in a column of 1 m^2 along the signal path from the satellite to the receiver (commonly referred to as Total Electron Content, TEC). The Slant TEC (STEC) is a quantity which is dependent on the ray path geometry from the satellite to the receiver through the ionosphere. Using thin shell approximation advanced

* Corresponding author.
E-mail address: valencehabyarimana@gmail.com (V. Habyarimana).

https://doi.org/10.1016/j.asr.2020.02.005
0273-1177/© 2020 COSPAR. Published by Elsevier Ltd. All rights reserved.

by Klobuchar (1986), STEC is converted to vertical TEC (VTEC) at the ionospheric pierce point using a suitable mapping function. While TEC can be directly derived from Global Navigation Satellite System (GNSS) observations, some regions (such as African low latitudes) are sparsely covered with GNSS receivers and hence mapping such regions becomes somewhat difficult. Thus there is a need to develop TEC models to simulate the low latitude ionosphere. Most of the available models such as International Reference Ionosphere (IRI) and NeQuick are climatological in nature (e.g. Bent et al., 1971; Hochegger et al., 2000; Radicella and Leitinger, 2001; Bilitza, 2001; Leitinger et al., 2005; Nava et al., 2008; Jakowski et al., 2011) and may not effectively represent the day to day changes in ionospheric electron density over the African low latitude regions (e.g. Brown et al., 1991; Batista et al., 1994; Mazzella et al., 2002; Coïsson et al., 2006; Jakowski et al., 2011). It has been previously stated that station-specific local models are necessary for precise application of satellite communication and navigation systems (Baruah et al., 1993; Gulyaeva, 1999; Ratnam and Sarma, 2006; Rao, 2007; Hajra et al., 2016; Sabzehee et al., 2018).

In most cases, single station empirical TEC models use seasonal and diurnal variations, and solar and geomagnetic activities as inputs (e.g. Habarulema et al., 2007; Uwamahoro and Habarulema, 2015; Eyelade et al., 2017; Song et al., 2018; Uwamahoro et al., 2018; Tebabal et al., 2018; Andima et al., 2019). In this paper, we have investigated the vertical $\mathbf{E}\times\mathbf{B}$ drift as an additional input during TEC modelling over a single station Mbarara (MBAR, $0.6°S$, $30.74°E$; $10.22°S$ geomagnetic) within the African low latitude region. Understanding the role played by vertical $\mathbf{E}\times\mathbf{B}$ drift in TEC variability is of paramount importance since vertical drifts dominate the electrodynamics of the low latitude region. Vertical $\mathbf{E}\times\mathbf{B}$ drift arises due to interaction between the day time eastward electric field and magnetic field of the Earth (Kelley, 2009), resulting in the uplift of the plasma which, under the influence of gravity and pressure gradient forces, diffuses to latitude regions within $\pm15°$ off the geomagnetic equator. When the ionosphere is lifted up to higher altitudes where recombination rate is low, the plasma stays there considerably longer leading to increase in electron density. Since TEC is an integration of the number of electrons along a ray path from the satellite to the receiver, TEC will be enhanced as a result of an enhancement in vertical $\mathbf{E}\times\mathbf{B}$ drift (Kelley, 2009). Thus, vertical $\mathbf{E}\times\mathbf{B}$ drift is an important driver of ionospheric morphology in the low latitude region (e.g. Mikhailov et al., 2007; Mikhailov et al., 2009; Kil et al., 2009; Siddiqui et al., 2015). Furthermore, the extent to which the ionosphere is uplifted under the influence of vertical $\mathbf{E}\times\mathbf{B}$ drift during both geomagnetically quiet and disturbed conditions needs to be understood (Oh et al., 2008). To properly model the low latitude ionosphere, there is a need for realistic vertical $\mathbf{E}\times\mathbf{B}$ drift data. The well known vertical $\mathbf{E}\times\mathbf{B}$ drift climatological model developed by Scherliess and Fejer (1999) using Jicamarca data and incorporated in International reference ionosphere (IRI) model provides monthly average vertical $\mathbf{E}\times\mathbf{B}$ drift data and may therefore not capture some local region-specific features. In the past, vertical $\mathbf{E}\times\mathbf{B}$ drift data has been very scarce in many longitude regions (e.g. McNamara, 1985; Fejer et al., 2008; Maini and Agrawal, 2011; Fejer et al., 2013; Dubazane and Habarulema, 2018). With the advent of satellite technology, vertical $\mathbf{E}\times\mathbf{B}$ drift data was obtained from the first Republic of China Satellites (ROCSAT-1) (e.g. Fejer et al., 2008; Kil et al., 2009), Challenging Mini-satellite Payload (CHAMP) (e.g. Lühr et al., 2004; Alken and Maus, 2007), Communication Navigation Outage and Forecasting System (C/NOFS) (e.g. Stoneback et al., 2011; Fejer et al., 2013; Dubazane and Habarulema, 2018; Marew et al., 2019) and SWARM (e.g. Oberheide et al., 2015; Lomidze et al., 2018) satellites, which sample all longitude sectors. Hence, in this study, we used C/NOFS satellite data to generate long-term vertical $\mathbf{E}\times\mathbf{B}$ drift over a single station based on non-linear approach, which is then used as an input in TEC modelling. The need to first develop a vertical $\mathbf{E}\times\mathbf{B}$ drift model based on C/NOFS data was necessitated by lack of ground-based instrumentation to provide continuous vertical drift data over the African region.

Efforts have been made to model TEC and validate the existing climatological models over African (e.g. Olwendo et al., 2012, 2013; Nigussie et al., 2016; Okoh et al., 2016; Andima et al., 2019; Uwamahoro et al., 2019), Brazilian (e.g. Leandro and Santos, 2007; Takahashi et al., 2014; Ferreira et al., 2017a; Ferreira et al., 2017b), Indian (e.g. Sethi et al., 2011; Prasad et al., 2012; Sur and Paul, 2013; Dabbakuti and Ratnam, 2017), and China (e.g. Mao et al., 2008; Song et al., 2018; Feng et al., 2019) low latitude regions. For example, Okoh et al. (2016) constructed a regional GNSS-VTEC model over Nigeria using Neural network (NN) approach. The authors used critical frequency of F2 layer (f_oF2) from IRI model as an additional input to help the network to learn long term solar cycle variations. Their model output had a reduction in prediction errors to about half those of the NeQuick and IRI models. Recently, Andima et al. (2019) constructed a GPS-TEC single station model based on empirical orthogonal function (EOF) approach and compared their results with the already existing IRI-2016 model and Global Ionospheric Maps data from Centre for Orbit Determination in Europe. Their reconstructed EOF-based TEC model generally modelled TEC with an accuracy of 50% better than IRI-2016 model. Very recently, Uwamahoro et al. (2018, 2019)developed storm-time models over the African low, equatorial and mid-latitude regions. Their results showed improvement in TEC modelling over climatological IRI model by about 58% for low latitude regions. Ferreira et al. (2017a) carried out a short term estimation of GNSS-TEC using NN model. The authors reported the network's ability

to forecast one day TEC data immediately after the period considered for the model development. Dabbakuti and Ratnam (2017) used EOF approach to reconstruct TEC over Bangalore in India and validated their models during high and low solar activity years. They found out that the observed TEC exhibited a good linear correlation with modelled TEC during high solar activity years in comparison with low solar activity period.

Empirical global, regional and single station approaches based on different techniques and set of inputs all point to a common conclusion of the need to improve TEC modelling especially in low/equatorial regions which exhibit complexities related to both ionospheric dynamics and electrodynamics. Thus, we present a study that has investigated inclusion of vertical drift as an input to TEC modelling over the African region for the first time. The TEC model was developed with a time resolution of 5 min based on GNSS data and a set of physical/geophysical parameters over MBAR (10.22°*S*, geomagnetic) covering a period of 2001–2015.

2. Data sources and selection of model inputs

2.1. Model inputs

TEC data was derived from Receiver INdependent Exchange (RINEX) observations (downloaded from ftp://data-out.unavco.org/pub/rinex/obs/) over the GNSS station, MBAR. The RINEX data was processed using GPS-TEC analysis software developed at Boston College (Seemala and Valladares, 2011). An elevation angle threshold of 30° was used to remove or minimise effects due to multipath. Fig. 1 shows availability of TEC data over MBAR from 2001 to 2015.

From Fig. 1, both the descending phase of solar cycle 23 (2004–2006) and the maximum phase of solar cycle 24 (2012–2014) had a fair data coverage compared to other years. In total, 940784 data points at an interval of 5 min (accounting for 59.6% of the expected data) were available for TEC model development.

TEC varies with solar activity and thus the solar activity dependence was represented by solar activity factor ($F10.7P$). Due to lack of a proper extreme ultraviolet (EUV) database (Doherty et al., 2000; Mahajan and Dwivedi, 2005), solar flux (F10.7) index (available at https://omniweb.gsfc.nasa.gov/form/dx1.html) can be used to represent solar activity variations (Chen et al., 2011; Hajra et al., 2016). Daily $F10.7P$ was calculated using Eq. (1).

$$F10.7P = \frac{F10.7 + F10.7_{81}}{2}, \quad (1)$$

where $F10.7_{81}$ is the 81 day running average of F10.7. Liu et al. (2006) demonstrated that $F10.7P$ gives a better representation of solar activity than F10.7 in ionospheric modelling. Fig. 2 shows the long-term relationship between TEC and $F10.7P$ for 2000–2016 at 1000 UT when we expect high values of ionospheric electron density. Apart from the period of prolonged solar minimum (2008–2010), TEC generally has a linear relationship with $F10.7P$. During the extended solar minimum period, the relationship between solar EUV and $F10.7P$ differed from that of the previous solar minimum periods (Chen et al., 2011) and this caused a remarkable change in ionospheric parameters.

The ionospheric electron density and hence TEC changes with variations in geomagnetic conditions. TEC usually responds in form of increase or decrease during geomagnetic storms (Essex et al., 1981; Prölss, 1993, 1995; Amabayo et al., 2012; D'ujanga et al., 2013; Matamba et al., 2015). The geomagnetic activity influence on the variation of TEC was accounted for using the symmetric component of the ring current, SYM-H index (https://omniweb.gsfc.nasa.gov/form/omni_min.html). The SYM-H is a high-time resolution geomagnetic activity index (Iyemori, 1990; Iyemori and Rao, 1996; Le et al., 2011) which is similar to the commonly used hourly Disturbance storm time (Dst) index (Sugiura and Kamei, 1991; Wanliss and Showalter, 2006; Le et al., 2011).

The diurnal and seasonal variation of TEC in our modelling procedure was represented by hour of the day (HR) and day number of year (DN) respectively.

2.2. Estimation of vertical $\boldsymbol{E}\times\boldsymbol{B}$ drift

Vertical $\mathbf{E}\times\mathbf{B}$ drift drives plasma fountain upwards and thus modifies the electron density structure of the ionosphere. We first used non-linear NN approach to model vertical $\mathbf{E}\times\mathbf{B}$ drift based on C/NOFS ion plasma drift velocity data obtained from: http://spdf.gsfc.nasa.gov/pub/data/cnofs/cindi/. The spatial coverage of C/NOFS data for this study was within a magnetic latitude range of ±5° centred at the geomagnetic latitude (−10°) of MBAR and a geographic longitude range of 30°–45° which accounts for a longitude range of 15 degrees to ensure that there is no local time effect on the results. The C/NOFS satellite ion plasma drift velocity within an altitude range of 400–550 km is equivalent to the vertical $\mathbf{E}\times\mathbf{B}$ drift (Stoneback et al., 2011; Yizengaw et al., 2014). The C/NOFS satellite operated between 2008 and 2015 which is the period that was used to develop the vertical $\mathbf{E}\times\mathbf{B}$ drift model. The developed vertical $\mathbf{E}\times\mathbf{B}$ drift model was used to reconstruct an extended vertical $\mathbf{E}\times\mathbf{B}$ drift database from 2001–2015, the period during which TEC data was available. Using the input parameters and procedure in Khadka et al. (2016) and Dubazane and Habarulema (2018), we have developed a NN model to reconstruct vertical $\mathbf{E}\times\mathbf{B}$ drift from C/NOFS ion drift data. The input space consisted of diurnal and seasonal variations, geomagnetic and solar activity changes. DN was used to represent seasonal variability while HR accounted for diurnal changes. HR and DN were each split into trigonometrical components of sine and cosine to allow data continuity (Williscroft and Poole, 1996; Oyeyemi et al., 2005;

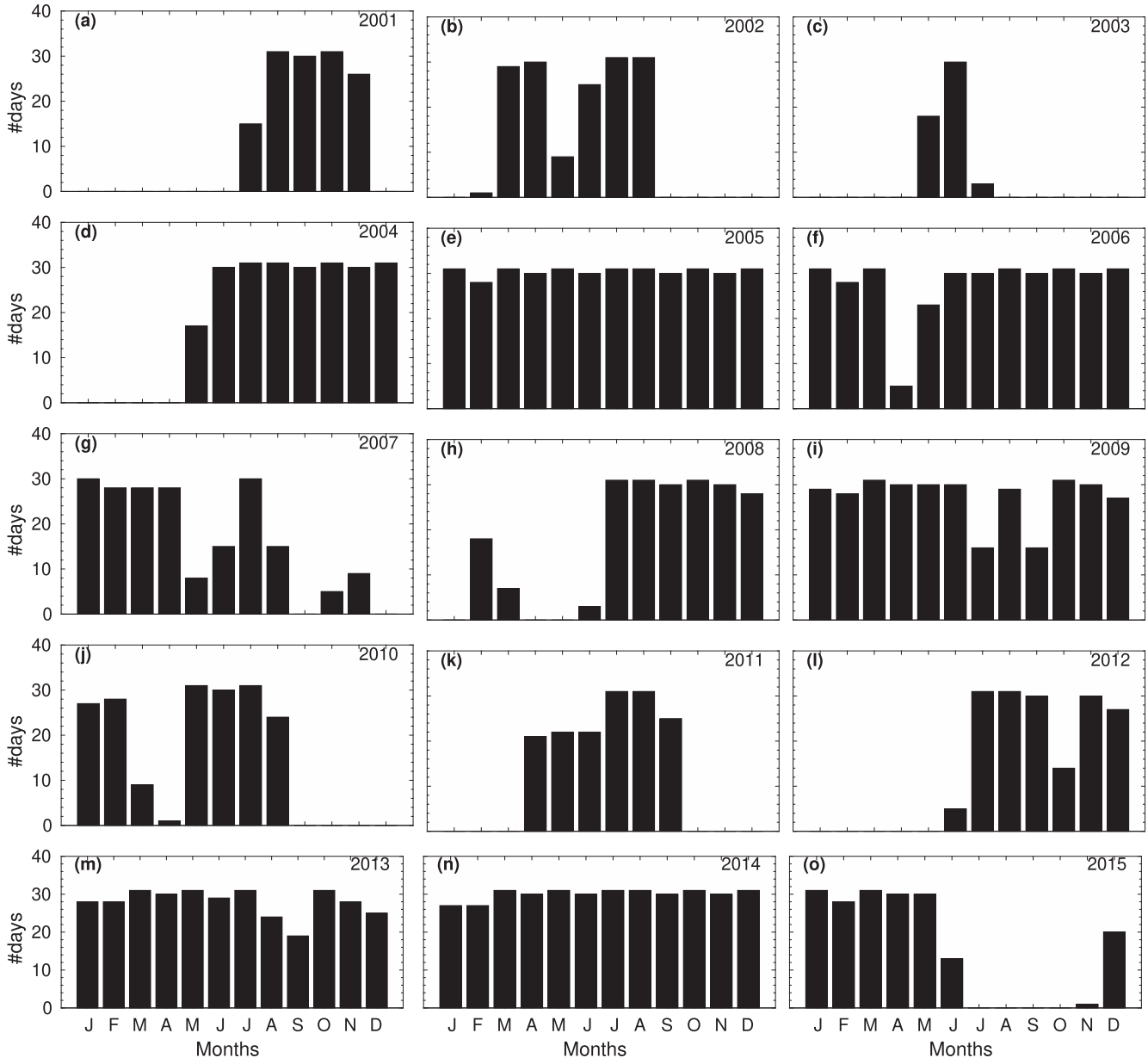


Fig. 1. Availability of TEC data over Mbarara used for model development from (a) 2001- (o) 2015.

Habarulema et al., 2007; Uwamahoro and Habarulema, 2015; Tshisaphungo et al., 2018), using Eq. (2).

$$\begin{aligned} dnsa &= sin\left(\tfrac{2\pi\times DN}{365.25}\right) \qquad dnca = cos\left(\tfrac{2\pi\times DN}{365.25}\right) \\ dnss &= sin\left(\tfrac{4\pi\times DN}{365.25}\right) \qquad dncs = cos\left(\tfrac{4\pi\times DN}{365.25}\right) \\ hrs &= sin\left(\tfrac{2\pi\times HR}{24}\right) \qquad hrc = cos\left(\tfrac{2\pi\times HR}{24}\right), \end{aligned} \tag{2}$$

where *dnsa* and *dnca* are inputs for annual variations, *dnss* and *dncs* are for semiannual variations, and *hrs* and *hrc* cater for the diurnal variations. The dataset consisting of all inputs and output parameters was divided into training, testing and validation in preparation for the development of a feed forward NN model. The Feedforward training process involves three stages: feedforward of the training pattern, calculation of the back-propagation of associated error, and weight adjustment (Fausett, 1994). During training, the network adjusts the weights of the connections until when a minimum error between the actual and modelled data is obtained (Oyeyemi et al., 2005; Song et al., 2018). When developing the model for estimation of vertical drifts, the NN was trained with data consisting of inputs and corresponding C/NOFS vertical **E**×**B** drift. The developed models for a number of hidden nodes were tested on data not used during training and the accuracy of the models computed using the actual and predicted **E**×**B** drift data. The veracity of the modelled vertical **E**×**B** drift was established using root mean square error (RMSE) between the model output and the C/NOFS vertical **E**×**B** drift. The minimum RMSE of the model was obtained

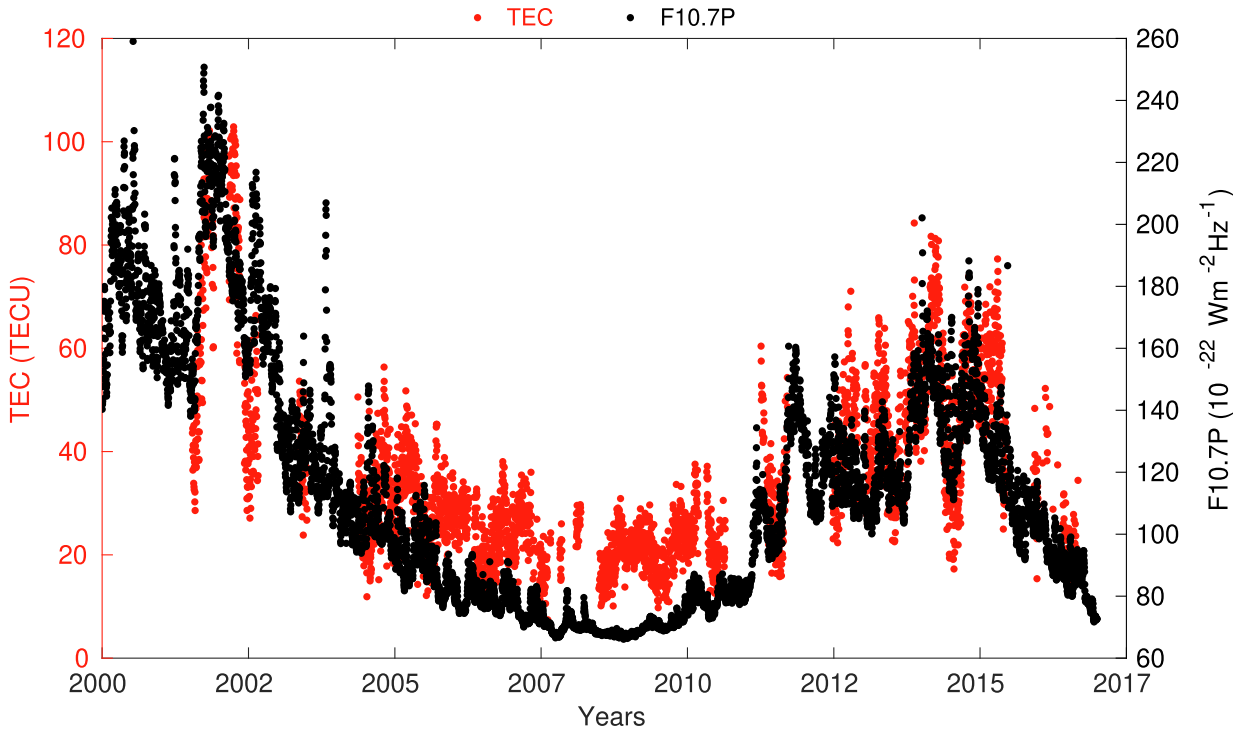


Fig. 2. Comparison of TEC at 1000 UT with long term $F10.7P$ from 2000–2016. The black and red dots represent $F10.7P$ and TEC values respectively. (For interpretation of the references to colour in this figure legend, the reader is referred to the web version of this article.)

after training with 10 hidden neurons. This method is commonly used while determining the number of hidden neurons for NN models (Hsu et al., 1995; Mohandes et al., 1998; Oyeyemi et al., 2005; Sabzehee et al., 2018). Hence the vertical **E**×**B** drift model used to estimate the **E**×**B** drift input consisted of 9 input, 10 hidden and one output neurons respectively.

Fig. 3(a) shows the diurnal representation of the available C/NOFS vertical **E**×**B** drift data from 2008 to 2015. Superimposed in red solid line is the hourly running average vertical **E**×**B** drift. Fig. 3(b) shows modelled vertical **E**×**B** drift data within 2008–2015. Similar to Fig. 3(a), hourly running average vertical **E**×**B** drift data is represented by the red solid curve. In Fig. 3(a)–(b) pre-reversal enhancement (PRE) is well pronounced just after 1600 UT (1900 LT). The PRE is a regular feature that appears in the eastward electric field (upward plasma drift) near the sunset before the electric field reverses to the west (downward plasma drift) (Fejer et al., 1999; Eccles et al., 2015). This results into an uplift of the F region plasma profile from 100 to 200 km above its typical altitude (Fejer et al., 1999; Eccles et al., 2015). The developed vertical **E**×**B** drift model was used to generate modelled vertical **E**×**B** drift from 2001 to 2015 depicted by blue dots in Fig. 3(c). Superimposed on Fig. 3(c) is actual vertical **E**×**B** drift data (red dots) from 2008 to 2015 and $F10.7P$ (black dots). We need to point out that there is no ground-based instrument for continuous vertical drift observations, thus no archived data for vertical **E**×**B** drifts over the African low latitude region. The $F10.7P$ and C/NOFS vertical **E**×**B** drift demonstrated a linear relationship except during the period of prolonged solar minimum (2008–2010) where the two showed little or no correlation (Solomon et al., 2013; Perna and Pezzopane, 2016). Fig. 3(d) shows a scatter plot between actual and modelled vertical **E**×**B** drifts during 2008–2015 yielding a strong positive linear relationship (R = 0.722, N = 6024). Fig. 4 shows the percentage distribution (histogram) of the differences between the actual C/NOFS and modelled vertical **E**×**B** drifts from 2008 to 2015. The percentage distribution frequency was calculated using Eq. (3).

$$\text{Percentage distribution} = \frac{\text{Number of elements in each bin}}{\text{Total number of elements in all bins}} \times 100\%, \quad (3)$$

where the bins were divided at an interval of 5 m/s between the minimum and maximum values of the differences. The statistical analysis showed that the two varied with mean, $\mu = 0.2033$ m/s and standard deviation, $\sigma = 15.4035$ m/s. Within a range of ±20 m/s (where most of the differences lied), a percentage frequency of 81.8% was obtained, whereas 95% of the differences lied within 2σ interval. The estimated vertical **E**×**B** drift data plotted as blue dots in Fig. 3(c) was then used along with other inputs to investigate whether vertical drifts have a potential contribution to TEC modelling.

3. The NN TEC model

After selection of the model inputs that influence TEC, two models (without and with vertical **E**×**B** drift input) were developed using NN approach. The inputs for the first

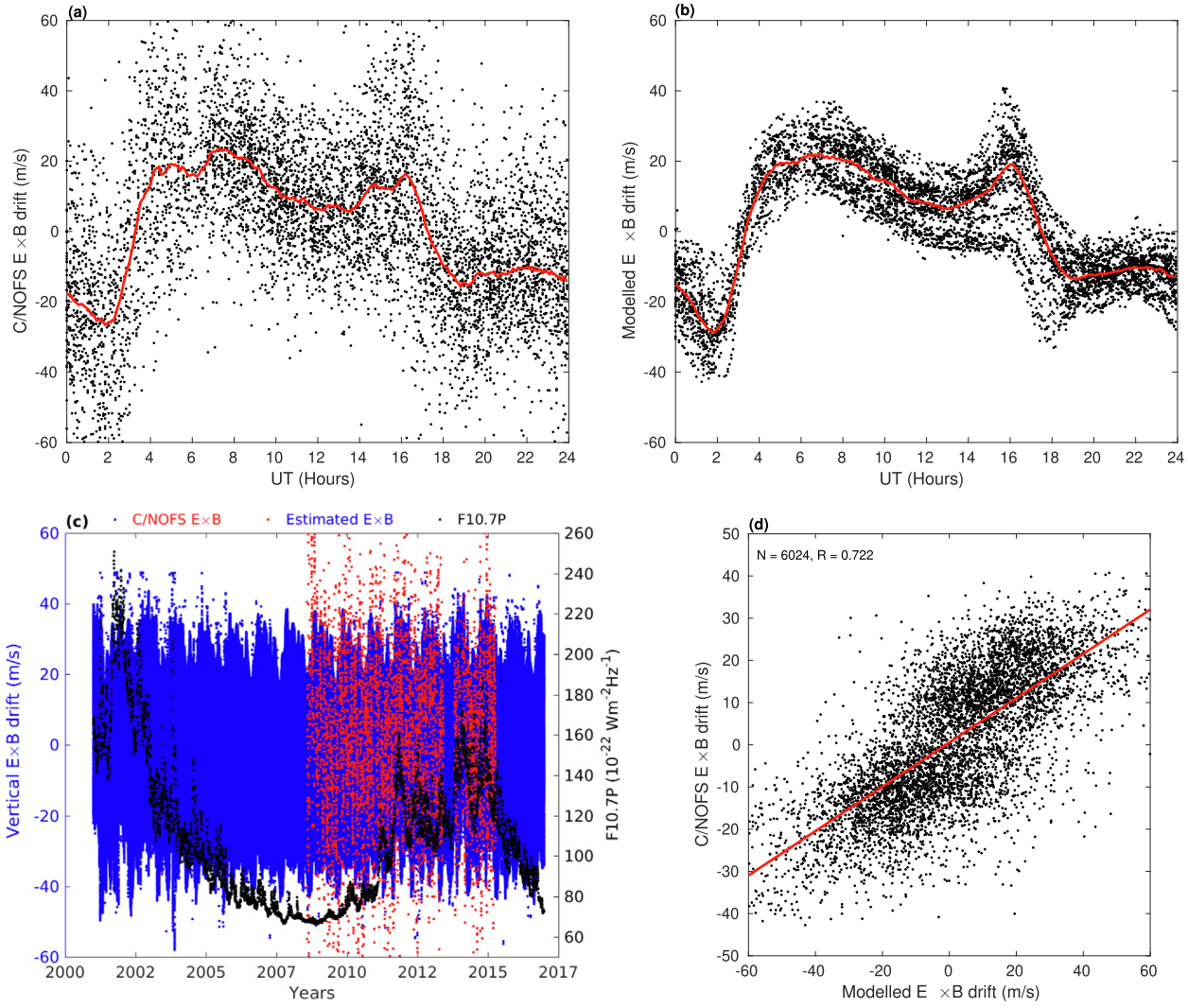


Fig. 3. Representation of the (a) diurnal variability of C/NOFS vertical **E**×**B** drift from 2008 to 2015, (b) diurnal variability of the modelled vertical **E**×**B** drift, (c) validation of the modelled vertical **E**×**B** drift (in blue) using C/NOFS vertical **E**×**B** drift (in red), (d) scatter plot of the actual and modelled vertical **E**×**B** drift over Mbarara. Overplotted on the panels (a) and (b) (in red) is the hourly running average of the actual and modelled vertical **E**×**B** drifts respectively. Superimposed on panel (c), in black, is $F10.7P$ to represent the variability of vertical **E**×**B** drift with solar activity. (For interpretation of the references to colour in this figure legend, the reader is referred to the web version of this article.)

model were diurnal and seasonal variations represented by different cyclic components in Eq. (2), solar activity ($F10.7P$) and geomagnetic activity (SYM-H index). Both diurnal and seasonal representations accounted for 6 inputs. Thus in total, the first model had 8 inputs. The second model had all the inputs as for the first model in addition to vertical **E**×**B** drift. The TEC data together with either 8 or 9 inputs' data from 2001 to 2015 was divided into training (90%), testing (5%) and validation (5%) datasets. Before developing the models, some data representing ascending, descending and maximum solar activity periods was removed and reserved for model verification. The first priority for the selection of the independent validation dataset was given to equinox and solstice days, but whenever these days had missing data, a substitution using any other day in the season would be made. For this, data for 16 days was reserved for final verification of the models' accuracy. Outside the 2001–2015 data range, we have tested the models using TEC data for 2016. The NN training was performed starting with the initial number of hidden neurons as 8 followed by increments in intervals of 1. After each set of hidden neurons, the accuracy of the model was computed using the mean absolute error (MAE) method. This process was repeated for hidden neurons ranging from 8 to 18. We selected MAE as an evaluation metric for our TEC models because it is a more natural measure of average error, unambiguous (Willmott and Matsuura, 2005) and less sensitive to outliers. In MAE, the error is calculated as an average of absolute differences between the target values and the predictions. The MAE is a linear score which means that all the individual differences are weighted equally in the average. The MAE was calculated using Eq. (4) (Mitchell and Spencer, 2003).

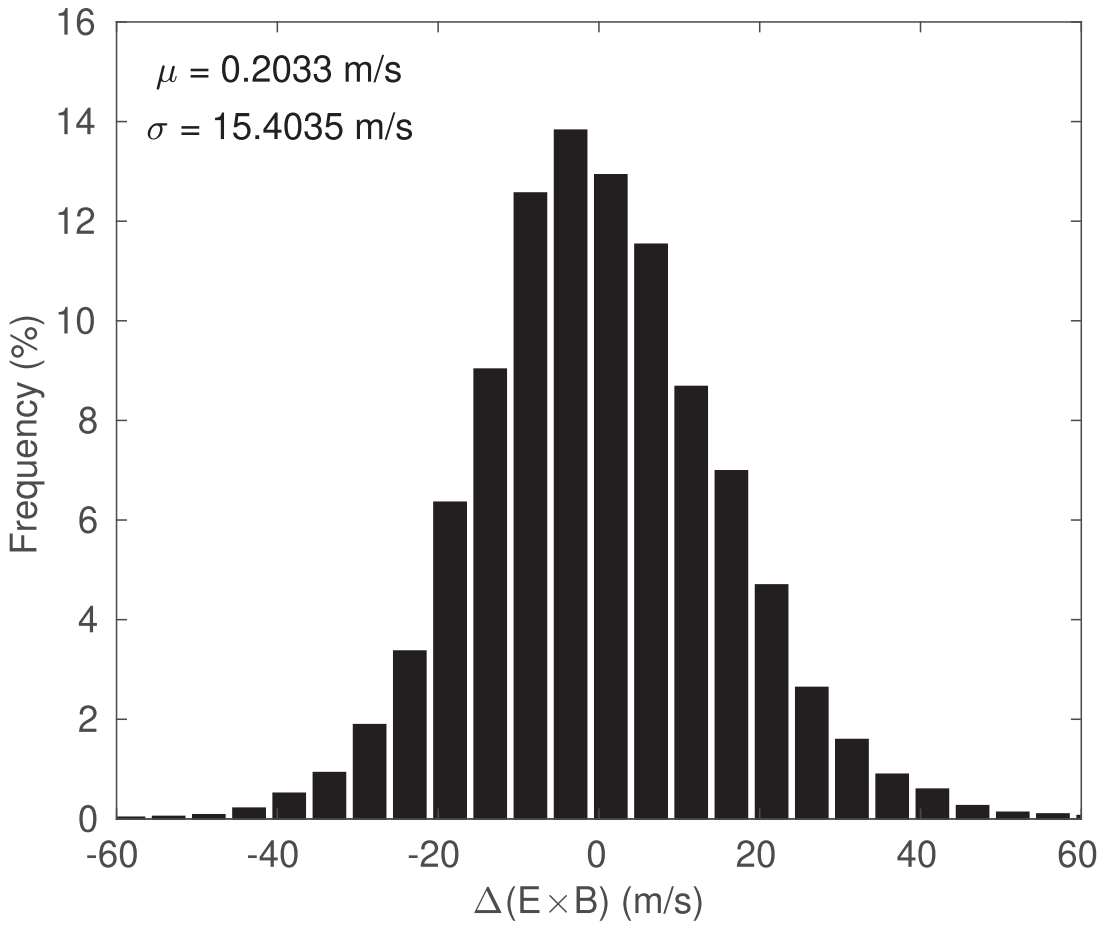


Fig. 4. Distribution of vertical **E**×**B** drift differences between the actual and modelled values from 2008 to 2015.

$$MAE = \frac{1}{N}\sum_{i=1}^{N}|TEC_{A_i} - TEC_{M_i}| \quad (4)$$

where TEC_{A_i} and TEC_{M_i} are the i^{th} actual and modelled TEC respectively. Fig. 5 shows the MAEs obtained from the model output and the actual data during models' development.

There is no standard procedure of selecting the best NN model (Simpson, 1990; Sheela and Deepa, 2013; Sabzehee et al., 2018). This is particularly critical for the choice of

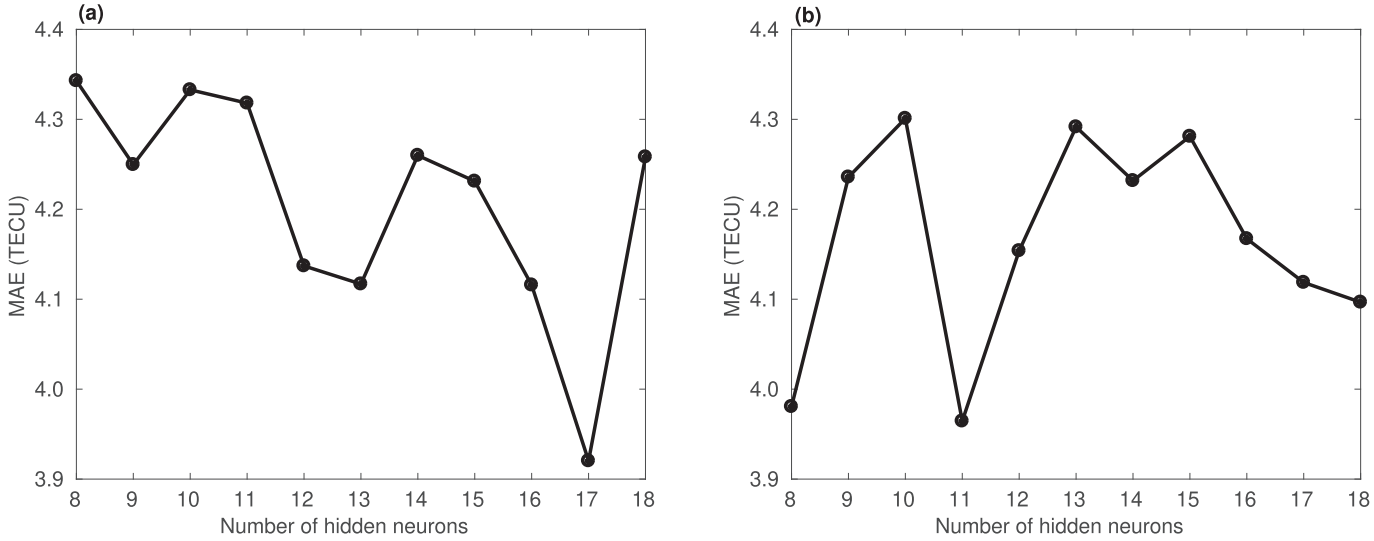


Fig. 5. MAE (a) without, and (b) with vertical **E**×**B** drift input for TEC models with varying number of hidden neurons between 8 and 18.

the number of hidden nodes which has been described as best done through the trial and error process (e.g. Yuan et al., 2010). Previous studies have used different statistical measures and taken the number of hidden neurons that best minimizes the error between actual and modelled data (e.g. Oyeyemi et al., 2005; Habarulema et al., 2007; Okoh et al., 2016; Khadka et al., 2016; Uwamahoro et al., 2018). In most cases, the number of hidden neurons that provide the first minimum value of the statistical accuracy measure is taken to ensure that the model generalizes the problem as opposed to memorization. The model architecture was determined by gradually changing the number of hidden neurons, computing the statistical accuracy and following the error minimization procedure between the modelled and actual data. An increase following series of consistent decrease in the error may be an indication that the choice of the optimum number of hidden neurons has been reached as further training may lead to over-fitting. As earlier mentioned, the determination of the "correct number of hidden neurons" is still a subjective area in neural network research and therefore different numbers of hidden nodes may be selected for the same model depending on the criteria followed. Nevertheless, from Fig. 5(a) the number of neurons which gave us the minimum MAE was 13 and hence taken as the generalised NN TEC model for the case without vertical **E**×**B** drift as an input. When the vertical **E**×**B** drift input was included, the first minimum MAE was obtained with 11 hidden neurons as shown in Fig. 5(b). Thus the model without vertical drift representation consisted of 8 input neurons corresponding to 8 input parameters, 13 hidden neurons which were statistically determined and 1 output neuron for TEC. For the second model which included vertical **E**×**B** drift, input and hidden neurons changed to 9 and 11 respectively; while the output neuron remained as 1.

4. Results and discussion

Fig. 6 shows the diurnal variability of TEC from the randomly selected days that were used to validate the models.

During model validation, in Fig. 6, periods were selected from solstice (June and December) and equinox (March and September) seasons. Where data were not available for the periods when equinoxes and solstices occurred in given months, any day was randomly selected within the affected season and reserved for validation. From Fig. 6, different phases of the solar cycles 23 and 24 were represented during validation. 2002 (177 sfu) and 2014 (144 sfu) were chosen as solar maximum years while 2005 (91 sfu) and 2008 (69 sfu) represented the descending and ascending phases respectively. To compliment MAE, we have also computed the correlation coefficient (R) and percentage deviations (PD) between modelled and observed TEC data. PD measures the degree to which individual data points in a statistic deviate from the average measurement of that statistic. To calculate PD, we used Eq. (5) (Akala et al., 2013; Song et al., 2018).

$$PD = \frac{1}{N}\sum_{i=1}^{N}\frac{|TEC_{A_i} - TEC_{M_i}|}{TEC_{A_i}} \times 100\%, \quad (5)$$

where TEC_{A_i} and TEC_{M_i} are as previously defined in Eq. (4). Table 1 shows a summary of these statistical parameters for data plotted in Fig. 6 during 2002, 2005, 2008 and 2014.

The average MAE calculated for all the validation dataset that generated Fig. 6 was 4.013 (3.757) TECU for the model without (with) vertical **E**×**B** drift input, accounting for an average percentage improvement of 6.4%. From Table 1, the inclusion of vertical **E**×**B** drift input led to improvement in TEC modelling for all periods except in 2005. High improvement (12.6%) is seen in 2002 followed by 2008 (6.9%) and then 2014 (4.6%); while 2005 showed a degradation in model performance. Given that the model showed some improvement in 2008 which fell within the prolonged solar minimum period, it is not clear why the results were negative for 2005. With this shortcoming, it is however appropriate to conclude that the inclusion of vertical **E**×**B** drift as an input may have the potential to improve empirical TEC modelling in low latitude regions. The PD of the model with vertical **E**×**B** drift input was on average 25.4% compared to 26.2% for the model without vertical **E**×**B** drift input. Fig. 7 shows the scatter plots between the actual and modelled TEC during the validation period. The correlation coefficient for the model without (with) vertical **E**×**B** drift input was 0.954 (0.958), showing a slight improvement.

To investigate the models' ability to reproduce the expected seasonal patterns, we have considered the year 2016 for two reasons. Over MBAR, 2016 data was sparsely available and therefore this provided an opportunity to examine the models' capability of filling the data gaps. Secondly, the model development utilized 2001–2015 data and therefore 2016 data would act as testing dataset for the limitations of the models in extrapolating TEC data in time. Fig. 8(a) and (b) show the available and modelled TEC data at 0800 UT (1100 LT) and 2000 UT (2300 LT) respectively for the year 2016 over MBAR. The MAE and R values for the models with and without vertical **E**×**B** drift input are indicated in the figure in black and blue colors respectively. These two time periods were chosen to assess the models' abilities in capturing TEC variability during periods when the ionospheric electron density is expected to depict relatively high and low values. While there is no data to validate the models' accuracy especially during March and September equinoxes, we note that the models reproduce the expected trend in TEC variability for these seasons. For the 0800 UT and 2000 UT, the June solstice is well modelled where data exists. The plots in Fig. 8(a)–(b) show highly pronounced annual and semi annual variations, and equinoctial asymmetry (Yonezawa, 1971; Mungufeni et al., 2016; Song et al., 2018). For the available data over MBAR, statistical analysis (especially the MAE values)

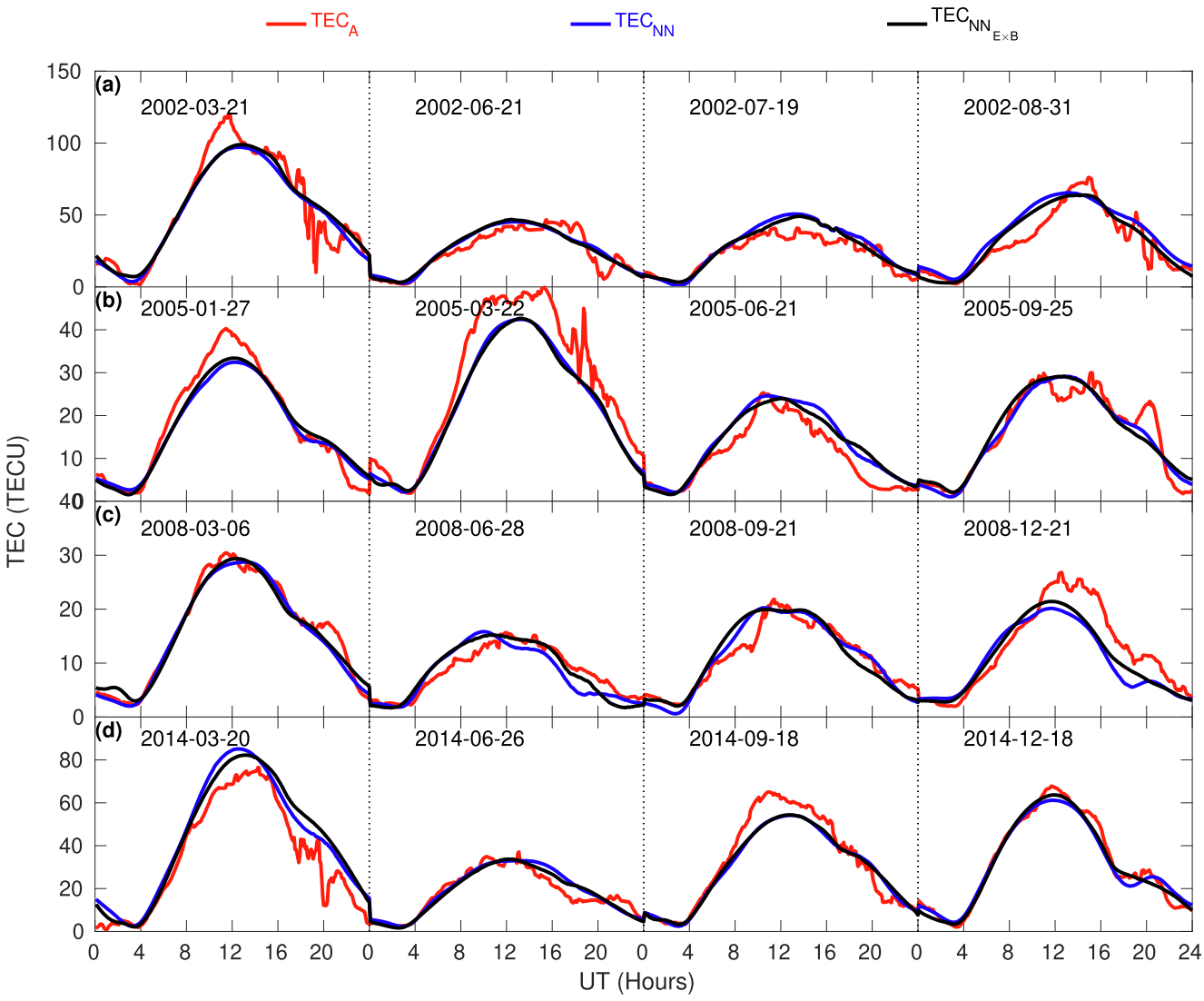


Fig. 6. Model validation during equinoxes and solstices for (a) 2002, (b) 2005, (c) 2008, and (d) 2014. The red solid curve represents the actual TEC (TEC_A) over MBAR. The blue and black curves represent the TEC model without (TEC_{NN}) and with ($TEC_{NN_{E\times B}}$) vertical **E**×**B** drift input respectively. (For interpretation of the references to colour in this figure legend, the reader is referred to the web version of this article.)

Table 1
Statistical analysis for validation dataset for each year. The values in brackets are for the model without vertical **E**×**B** drift input while the ones outside the brackets are for the model with vertical **E**×**B** drift input.

Year	MAE (TECU)	Improvement (%)	R	PD (%)
2002	5.601 (6.407)	12.6	0.958 (0.950)	27.3 (28.9)
2005	3.248 (3.117)	−4.2	0.962 (0.965)	29.6 (26.4)
2008	1.848 (1.985)	6.9	0.951 (0.941)	20.4 (20.9)
2014	4.332 (4.542)	4.6	0.959 (0.959)	24.4 (28.8)

shows that the accuracy of the two models is comparable with the model that has vertical **E**×**B** drift input sometimes providing some improvement. Because MBAR data was sparse in 2016, we used data from Eldoret in Kenya (MOIU, 0.29°N, 35.29°E; 9.19°S) which lies within the same longitude sector, to validate the seasonal dependencies depicted by the models in Fig. 8(a)–(b). Fig. 8(c)–(d) shows the data from MOIU (red dots) superimposed on the developed models at 0800 UT and 2000 UT respectively. The computed statistics show that at 0800 UT, using the MAE, the model with vertical **E**×**B** drift input performed 2% better than the one without. However, R values between each of the two models and TEC over MOIU was similar (0.776) using N = 325 ordered pairs. At 2000 UT, the calculated MAE was 6% greater for the model without than with vertical **E**×**B** drift input. The R values slightly reduced from 0.786 to 0.782 for the model without and with vertical **E**×**B** drift input respectively using 330 ordered pairs.

Overall, the developed models were able to capture the well known seasonal patterns even during cross validation using data from a nearby station. Previously, TEC modelling efforts have been presented (Anderson and Klobuchar, 1983; Anderson et al., 1987; Okoh et al., 2016; Ferreira et al., 2017a; Uwamahoro et al., 2018; Andima et al., 2019) and the reported accuracies in performance of the developed models lied within a range of 5–10

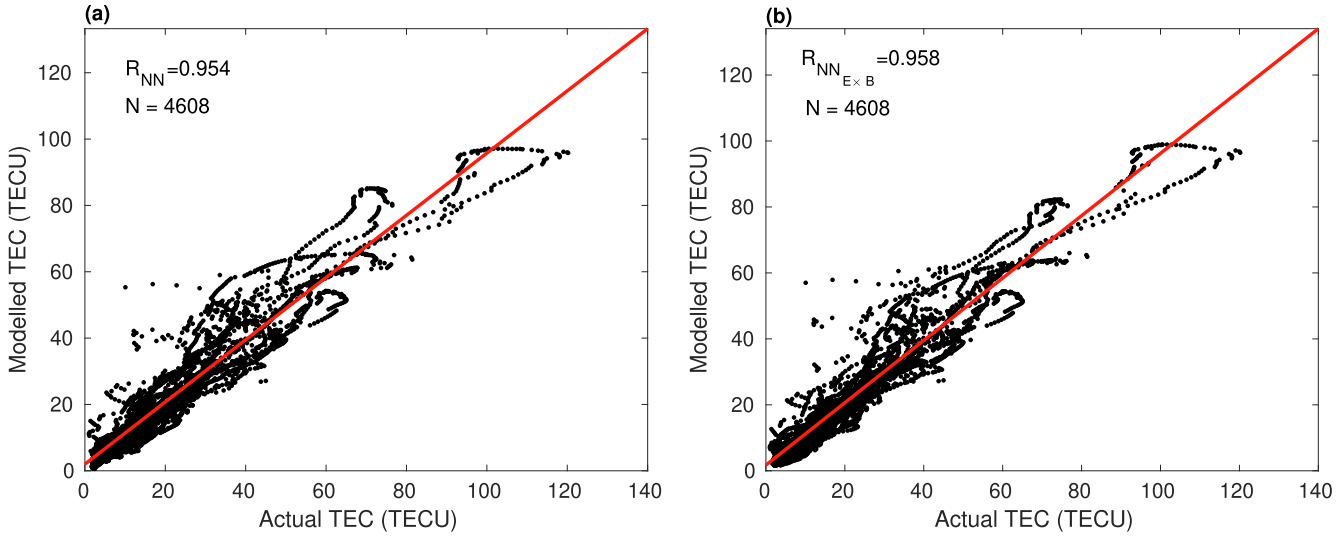


Fig. 7. Scatter plots between actual and modelled TEC values (a) without, (b) with vertical **E**×**B** drift input. R_{NN} and $R_{NN_{E\times B}}$ represent the correlation coefficients between the actual TEC and modelled TEC without and with vertical **E**×**B** drift input respectively, while N represents the number of points.

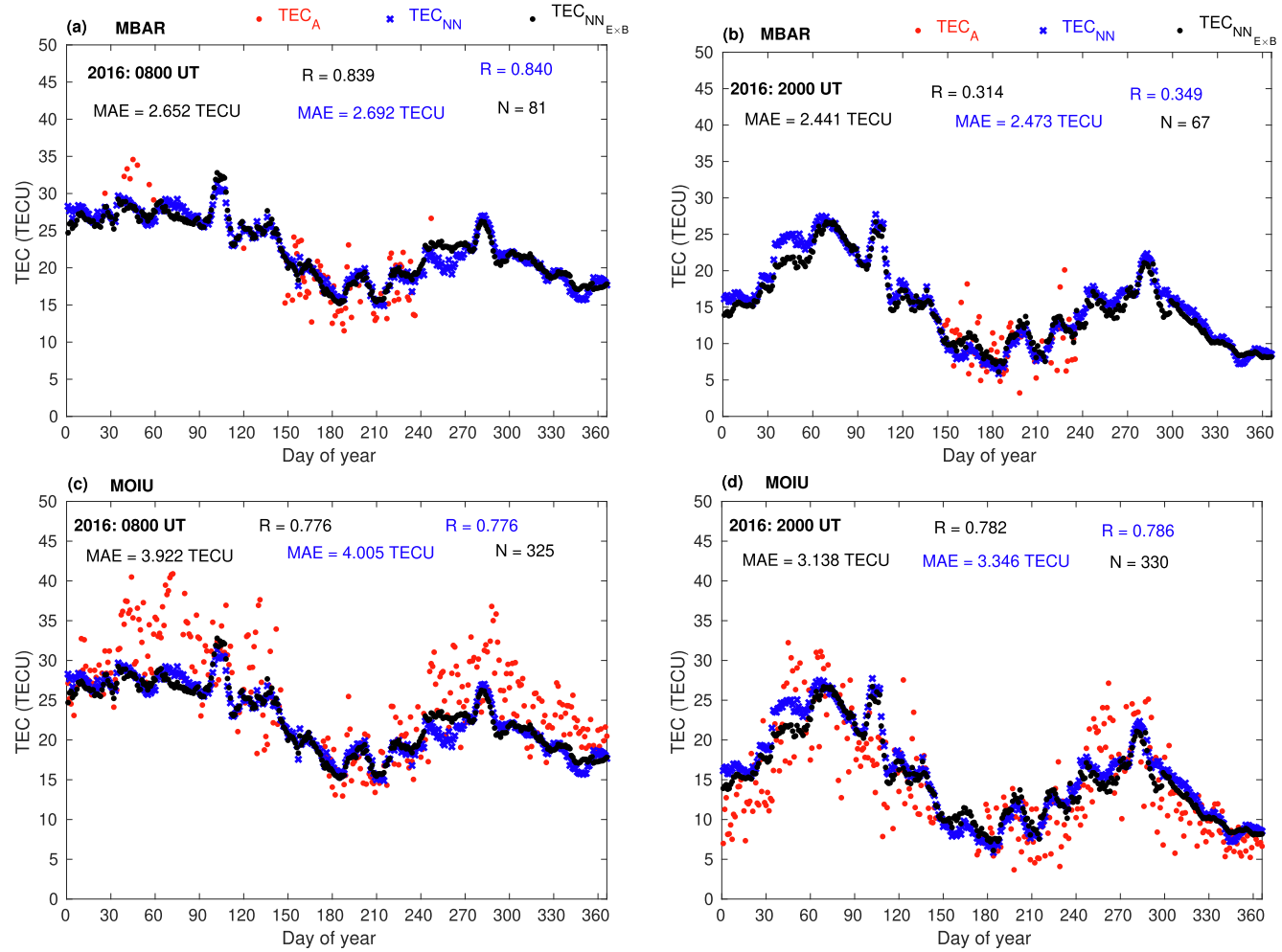


Fig. 8. Variation of actual and modelled TEC at 0800 UT and 2000 UT over (a)-(b) MBAR, (c)-(d) MOIU. The mean absolute error and correlation coefficients are shown on the graphs in black (blue) for the model with (without) vertical **E**×**B** drift input. TEC_A, TEC_{NN}, and $TEC_{NN_{E\times B}}$ represent the actual TEC, modelled TEC without and with vertical **E**×**B** drift input respectively. (For interpretation of the references to colour in this figure legend, the reader is referred to the web version of this article.)

TECU with the measured and modelled values being highly correlated. Our results are comparable and sometimes exhibit a higher accuracy when analyzed in context of existing studies. Due to limited single station TEC modelling studies over the African low latitude region, our comparison with existing literature also included regional modelling results. While it is expected that single station models outperform regional and global modelling efforts, our results are sometimes more accurate when compared to existing single station results over the African low latitude region (e.g. Uwamahoro et al., 2018; Uwamahoro et al., 2019; Andima et al., 2019). Our results have therefore been compared to previous single station studies and regional efforts especially over the African region (Okoh et al., 2016; Uwamahoro et al., 2018; Uwamahoro et al., 2019; Andima et al., 2019). For example, Okoh et al. (2016) reported average RMSE value of 8.5 TECU over Nigeria. Using a similar statistical measure, our verification results provide RMSE value of 5.85 TECU for the model without vertical **E**×**B** drift input. This value reduces to 5.72 TECU when vertical **E**×**B** drift is taken into account. On the other hand, validation during low and high solar activity years gave a range of RMSEs within 3.31–7.03 TECU in comparison with a maximum of 10 TECU obtained by Andima et al. (2019) during similar solar activity periods. During their TEC reconstruction, Uwamahoro et al. (2018) used the storm-time data over MBAR and obtained a smallest RMSE slightly above 6 TECU over MBAR. This value is slightly higher than 5.85 TECU arrived at in this current study. The MAE obtained by Uwamahoro et al. (2019) while validating their storm-time model over the low latitude region, is higher than the one in this current study by about 0.5 TECU. During their forecasting techniques in Brazil, Ferreira et al. (2017a) used NN approach and obtained a maximum RMSE of 7.9 TECU for one day immediately after the training period. Comparing this with our extrapolation carried out in 2016 for 330 days using TEC data over MOIU, an average RMSE of 7.2 TECU for the model without vertical **E**×**B** drift input was obtained. These are statistically comparable results, although we have done long term validation. The computed R values during the low and high solar activity periods before including vertical **E**×**B** drift input were similar (0.95). Dabbakuti and Ratnam (2017) validated their NN hourly TEC based models over Bangalore in India and obtained correlation coefficients of 0.99 and 0.98 during high and low solar activity years respectively. The observed slight difference in R values between our model and the one for Dabbakuti and Ratnam (2017) can be attributed to the differences in time resolution between the two models. These statistics show that our model is capable of estimating the ionospheric variations over the low latitude region. Hence, the model can be extended to include the rest of Africa and generate African TEC model for regional mapping with inclusion of vertical **E**×**B** drift input.

5. Conclusions

This paper presented a slightly improved TEC model over a single station when the vertical **E**×**B** drift input is taken into account. By using the vertical **E**×**B** drift data estimated from the C/NOFS satellite as an additional input into the TEC model, validation results showed improvement of about 6%. Correlation coefficient results similarly showed improvement from 0.954 to 0.958 when vertical **E**×**B** drift was included into the TEC model. Annual long extrapolation in 2016 at 0800 UT and 2000 UT when electron density values are at their relatively high and lowest respectively revealed that the models are reliable in showing expected seasonal features. Validation using the nearest GNSS station in Kenya (MOIU) revealed that the developed models may be used to generate TEC at the stations within the vicinity of MBAR, especially when there are data gaps. Hence, the model with vertical **E**×**B** drift input can be extended to map the African region and comprehend the importance of vertical **E**×**B** drifts in TEC modelling.

Acknowledgements

The first author extends his sincere gratitude to the African Development Bank-Higher Education for Science and Technology (AfDB-HEST) for funding this study. SANSA's conducive atmosphere during the research visit by the corresponding author is acknowledged. The provision of GPS-TEC software used to decompress the RINEX data developed at Boston College is acknowledged. The authors thank NASA and UNAVCO for the provision of data on their corresponding websites.

References

Abdu, M., 2001. Outstanding problems in the equatorial ionosphere–thermosphere electrodynamics relevant to spread F. J. Atmos. Solar Terr. Phys. 63 (9), 869–884.

Akala, A., Seemala, G., Doherty, P., Valladares, C., Carrano, C., Espinoza, J., Oluyo, S., 2013. Comparison of equatorial GPS-TEC observations over an African station and an American station during the minimum and ascending phases of solar cycle 24. Ann. Geophys. 31, 2085–2096.

Alken, P., Maus, S., 2007. Spatio-temporal characterization of the equatorial electrojet from CHAMP, Ørsted, and SAC-C satellite magnetic measurements. J. Geophys. Res.: Space Phys. 112 (A09305).

Amabayo, E.B., McKinnell, L.A., Cilliers, P.J., 2012. Ionospheric response over South Africa to the geomagnetic storm of 11–13 April 2001. J. Atmos. Solar Terr. Phys. 84, 62–74.

Anderson, D., Klobuchar, J., 1983. Modeling the total electron content observations above Ascension Island. J. Geophys. Res.: Space Phys. 88 (A10), 8020–8024.

Anderson, D.N., Mendillo, M., Herniter, B., 1987. A semi-empirical low-latitude ionospheric model. Radio Sci. 22 (2), 292–306.

Andima, G., Amabayo, E.B., Jurua, E., Cilliers, P.J., 2019. Modeling of GPS total electron content over the African low-latitude region using empirical orthogonal functions. Annales Geophysicae, Copernicus GmbH vol. 37, pp. 65–76.

Astafyeva, E., Zakharenkova, I., Hozumi, K., Alken, P., Coïsson, P., Hairston, M.R., Coley, W.R., 2018. Study of the equatorial and low-latitude electrodynamic and ionospheric disturbances during the 22–23 June 2015 geomagnetic storm using ground-based and spaceborne techniques. J. Geophys. Res.: Space Phys. 123 (3), 2424–2440.

Baruah, S., Bhuyan, P., Tyagi, T., 1993. Modelling of ionospheric electron content over Lunping-an empirical approach. Indian J. Radio Space Phys. 22, 325–330.

Batista, I., De Souza, J., Abdu, M., De Paula, E., 1994. Total electron content at low latitudes and its comparison with the IRI90. Adv. Space Res. 14 (12), 87–90.

Bent, R., Llewellyn, S., Schmid, P., 1971. Ionospheric refraction corrections in satellite tracking. Space Res. 12, 1186–1194.

Bilitza, D., 2001. International reference ionosphere 2000. Radio Sci. 36 (2), 261–275.

Brown, L.D., Daniell, R.E., Fox, M.W., Klobuchar, J.A., Doherty, P.H., 1991. Evaluation of six ionospheric models as predictors of total electron content. Radio Sci. 26 (4), 1007–1015.

Burke, W., Hardy, D., Rich, F., Sagalyn, R., Shuman, B., Smiddy, M., Vancour, R., Wildman, P., Kelley, M., Doyle, M., et al., 1984. High latitude electrodynamics: observations from S3–2. Space Sci. Rev. 37 (1–2), 161–200.

Chen, Y., Liu, L., Wan, W., 2011. Does the F10. 7 index correctly describe solar EUV flux during the deep solar minimum of 2007–2009?. J. Geophys. Res.: Space Phys. 116 (A4).

Coïsson, P., Radicella, S., Leitinger, R., Nava, B., 2006. Topside electron density in IRI and NeQuick: features and limitations. Adv. Space Res. 37 (5), 937–942.

Dabbakuti, J.K., Ratnam, D.V., 2017. Modeling and analysis of GPS-TEC low latitude climatology during the 24th solar cycle using empirical orthogonal functions. Adv. Space Res. 60 (8), 1751–1764.

Doherty, P.H., Klobuchar, J.A., Kunches, J.M., 2000. Eye on the ionosphere: the correlation between solar 10.7 cm radio flux and ionospheric range delay. GPS Solut. 3 (4), 75–79.

Dubazane, M.B., Habarulema, J.B., 2018. An empirical Model of vertical Plasma drift over the African sector. Space Weather 16 (6), 619–635.

D'ujanga, F., Baki, P., Olwendo, J., Twinamasiko, B., 2013. Total electron content of the ionosphere at two stations in East Africa during the 24–25 October 2011 geomagnetic storm. Adv. Space Res. 51 (5), 712–721.

Eccles, J., St. Maurice, J., Schunk, R., 2015. Mechanisms underlying the prereversal enhancement of the vertical plasma drift in the low-latitude ionosphere. J. Geophys. Res.: Space Phys. 120 (6), 4950–4970.

Essex, E., Mendillo, M., Schödel, J., Klobuchar, J., Da Rosa, A., Yeh, K., Fritz, R., Hibberd, F., Kersley, L., Koster, J., et al., 1981. A global response of the total electron content of the ionosphere to the magnetic storm of 17 and 18 June 1972. J. Atmos. Terr. Phys. 43 (4), 293–306.

Eyelade, V.A., Adewale, A.O., Akala, A.O., Bolaji, O.S., Rabiu, A.B., 2017. Studying the variability in the diurnal and seasonal variations in GPS total electron content over Nigeria. Annales Geophysicae, Copernicus GmbH, vol. 35, pp. 701–710.

Fausett, L.V. et al., 1994. Fundamentals of Neural Networks: Architectures, Algorithms, and Applications, Vol. 3. Prentice-Hall, Englewood Cliffs.

Fejer, B.G., 1981. The equatorial ionospheric electric fields. A review. J. Atmos. Terr. Phys. 43 (5–6), 377–386.

Fejer, B.G., Scherliess, L., De Paula, E., 1999. Effects of the vertical plasma drift velocity on the generation and evolution of equatorial spread F. J. Geophys. Res.: Space Phys. 104 (A9), 19859–19869.

Fejer, B.G., 2002. Low latitude storm time ionospheric electrodynamics. J. Atmos. Solar Terr. Phys. 64 (12–14), 1401–1408.

Fejer, B.G., Jensen, J.W., Su, S.Y., 2008. Quiet time equatorial F region vertical plasma drift model derived from ROCSAT-1 observations. J. Geophys. Res.: Space Phys. 113 (A5).

Fejer, B.G., 2011. Low latitude ionospheric electrodynamics. Space Sci. Rev. 158 (1), 145–166.

Fejer, B.G., Tracy, B.D., Pfaff, R.F., 2013. Equatorial zonal plasma drifts measured by the C/NOFS satellite during the 2008–2011 solar minimum. J. Geophys. Res.: Space Phys. 118 (6), 3891–3897.

Feng, J., Han, B., Zhao, Z., Wang, Z., 2019. A new global total electron content empirical model. Remote Sens. 11 (6), 706. https://doi.org/10.3390/rs11060706.

Ferreira, A.A., Borges, R.A., Paparini, C., Ciraolo, L., Radicella, S.M., 2017a. Short-term estimation of GNSS TEC using a neural network model in Brazil. Adv. Space Res. 60 (8), 1765–1776.

Ferreira, A.A., Borges, R.A., Paparini, C., Radicella, S.M., 2017b. TEC modelling via neural network using observations from the first GLONASS R&D data network in Brazil and the RBMC. IFAC-PapersOnLine 50 (1), 12829–12834.

Gulyaeva, T., 1999. Regional analytical model of ionospheric total electron content: monthly mean and standard deviation. Radio Sci. 34 (6), 1507–1512.

Habarulema, J.B., McKinnell, L.A., Cilliers, P.J., 2007. Prediction of global positioning system total electron content using neural networks over South Africa. J. Atmos. Sol.-Terrestr. Phys. 69 (15), 1842–1850.

Hajra, R., Chakraborty, S.K., Tsurutani, B.T., DasGupta, A., Echer, E., Brum, C.G., Gonzalez, W.D., Sobral, J.H.A., 2016. An empirical model of ionospheric total electron content (TEC) near the crest of the equatorial ionization anomaly (EIA). J. Space Weather Space Clim. 6, A29.

Heelis, R., 2004. Electrodynamics in the low and middle latitude ionosphere: a tutorial. J. Atmos. Solar Terr. Phys. 66 (10), 825–838.

Hochegger, G., Nava, B., Radicella, S., Leitinger, R., 2000. A family of ionospheric models for different uses. Phys. Chem. Earth, Part C: Solar, Terrestr. Planet. Sci. 25 (4), 307–310.

Hsu, K.L., Gupta, H.V., Sorooshian, S., 1995. Artificial neural network modeling of the rainfall-runoff process. Water Resour. Res. 31 (10), 2517–2530.

Iyemori, T., 1990. Storm-time magnetospheric currents inferred from mid-latitude geomagnetic field variations. J. Geomagn. Geoelectr. 42, 1249–1265.

Iyemori, T., Rao, D.R.K., 1996. Decay of the Dst field of geomagnetic disturbance after substorm onset and its implication to storm-substorm relation. Annals Geophys. 14, 608–618.

Jakowski, N., Mayer, C., Hoque, M., Wilken, V., 2011. Total electron content models and their use in ionosphere monitoring. Radio Sci. 46 (6).

Kelley, M.C., 2009. The Earth's Ionosphere: Plasma Physics and Electrodynamics, 96. Academic press.

Khadka, S.M., Valladares, C., Pradipta, R., Pacheco, E., Condor, P., 2016. On the mutual relationship of the equatorial electrojet, TEC and scintillation in the Peruvian sector. Radio Sci. 51 (6), 742–751.

Kil, H., Oh, S.J., Paxton, L.J., Fang, T.W., 2009. High-resolution vertical E×B drift model derived from ROCSAT-1 data. J. Geophys. Res.: Space Phys. 114 (A10).

Klobuchar, J.A., 1986. Design and characteristics of the GPS ionospheric time delay algorithm for single frequency users. In: PLANS'86-Position Location and Navigation Symposium, pp. 280–286.

Le, G., Burke, W.J., Pfaff, R.F., Freudenreich, H., Maus, S., Lühr, H., 2011. C/NOFS measurements of magnetic perturbations in the low-latitude ionosphere during magnetic storms. J. Geophys. Res. 116 (A12230).

Leandro, R., Santos, M., 2007. A neural network approach for regional vertical total electron content modelling. Stud. Geophys. Geod. 51 (2), 279–292.

Leitinger, R., Zhang, M.L., Radicella, S.M., 2005. An improved bottomside for the ionospheric electron density model NeQuick. Annals Geophys. 48 (3), 525–534.

Liu, L., Wan, W., Ning, B., Pirog, O., Kurkin, V., 2006. Solar activity variations of the ionospheric peak electron density. J. Geophys. Res.: Space Phys. 111 (A8).

Lomidze, L., Knudsen, D.J., Burchill, J., Kouznetsov, A., Buchert, S.C., 2018. Calibration and validation of Swarm plasma densities and electron temperatures using ground-based radars and satellite radio occultation measurements. Radio Sci. 53 (1), 15–36.

Lühr, H., Maus, S., Rother, M., 2004. Noon-time equatorial electrojet: Its spatial features as determined by the CHAMP satellite. J. Geophys. Res.: Space Phys. 109 (A1).

Mahajan, K., Dwivedi, A., 2005. Solar EUV flux during sunspot cycles 21, 22 and 23 -correlation with proxy indices and real time prediction. Indian J. Radio Space Phys. 34, 153–160.
Maini, A.K., Agrawal, V., 2011. Satellite Technology: Principles and Applications. John Wiley & Sons.
Mao, T., Wan, W., Yue, X., Sun, L., Zhao, B., Guo, J., 2008. An empirical orthogonal function model of total electron content over China. Radio Sci. 43 (02), 1–12.
Marew, H., Nigussie, M., Hui, D., Damitie, B., 2019. A method of estimating equatorial plasma vertical drift velocity and its evaluation using C/NOFS observations. Radio Sci. 54. https://doi.org/10.1029/2019RS006800.
Matamba, T.M., Habarulema, J.B., McKinnell, L.A., 2015. Statistical analysis of the ionospheric response during geomagnetic storm conditions over South Africa using ionosonde and GPS data. Space Weather 13 (9), 536–547.
Mazzella Jr, A.J., Holland, E.A., Andreasen, A.M., Andreasen, C.C., Rao, G.S., Bishop, G.J., 2002. Autonomous estimation of plasmasphere content using GPS measurements. Radio Sci. 37 (6). https://doi.org/10.1029/2001RS002520.
McNamara, L., 1985. The use of total electron content measurements to validate empirical models of the ionosphere. Adv. Space Res. 5 (7), 81–90.
Mikhailov, A., Depuev, V., Depueva, A., 2007. Synchronous NmF2 and NmE Daytime Variations as a Key to the Mechanism of Quiet-time F2-layer Disturbances. Ann. Geophys. 25, 483–493.
Mikhailov, A., Depueva, A., Depuev, V., 2009. Quiet time F2-layer disturbances: seasonal variations of the occurrence in the daytime sector. Ann. Geophys. 27, 329–337.
Mitchell, C.N., Spencer, P.S., 2003. A three-dimensional time-dependent algorithm for ionospheric imaging using GPS. Annals Geophys. 46 (4), 687–696.
Mohandes, M.A., Rehman, S., Halawani, T.O., 1998. A neural networks approach for wind speed prediction. Renew. Energy 13 (3), 345–354.
Mungufeni, P., Habarulema, J.B., Jurua, E., 2016. Trends of ionospheric irregularities over African low latitude region during quiet geomagnetic conditions. J. Atmos. Solar Terr. Phys. 138, 261–267.
Nava, B., Coisson, P., Radicella, S., 2008. A new version of the NeQuick ionosphere electron density model. J. Atmos. Solar Terr. Phys. 70 (15), 1856–1862.
Nigussie, M., Radicella, S., Damtie, B., Yizengaw, E., Nava, B., Roininen, L., 2016. Validation of NeQuick TEC data ingestion technique against C/NOFS and EISCAT electron density measurements. Radio Sci. 51 (7), 905–917.
Norsuzila, Y., 2008. Determination of GPS total electron content using single layer model ionospheric mapping function. Int. J. Comput. Sci. Network Secur. 8 (9), 1–7.
Oberheide, J., Shiokawa, K., Gurubaran, S., Ward, W.E., Fujiwara, H., Kosch, M.J., Makela, J.J., Takahashi, H., 2015. The geospace response to variable inputs from the lower atmosphere: a review of the progress made by Task Group 4 of CAWSES-II. Prog. Earth Planet. Sci. 2 (1), 2. https://doi.org/10.1186/s40645-014-0031-4.
Oh, S., Kil, H., Kim, W., Paxton, L., Kim, Y., 2008. The role of the vertical E×B drift for the formation of the longitudinal plasma density structure in the low-latitude F region. Ann. Geophys. 26 (7), 2061–2067.
Okoh, D., Owolabi, O., Ekechukwu, C., Folarin, O., Arhiwo, G., Agbo, J., Bolaji, S., Rabiu, B., 2016. A regional GNSS-VTEC model over Nigeria using neural networks: a novel approach. Geodesy Geodynam. 7 (1), 19–31.
Olwendo, O., Baki, P., Mito, C., Doherty, P., 2012. Characterization of ionospheric GPS Total Electron Content (GPS–TEC) in low latitude zone over the Kenyan region during a very low solar activity phase. J. Atmos. Solar Terr. Phys. 84, 52–61.
Olwendo, O., Baki, P., Cilliers, P., Mito, C., Doherty, P., 2013. Comparison of GPS TEC variations with IRI-2007 TEC prediction at equatorial latitudes during a low solar activity (2009–2011) phase over the Kenyan region. Adv. Space Res. 52 (10), 1770–1779.
Oyeyemi, E., Poole, A., McKinnell, L., 2005. On the global model for foF2 using neural networks. Radio Sci. 40 (6). https://doi.org/10.1029/2004RS003223.
Perna, L., Pezzopane, M., 2016. foF2 vs solar indices for the Rome station: Looking for the best general relation which is able to describe the anomalous minimum between cycles 23 and 24. J. Atmos. Solar-Terrestr. Phys. 148, 13–21.
Prasad, S., Rao, P.R., Prasad, D., Venkatesh, K., Niranjan, K., 2012. On the variabilities of the Total Electron Content (TEC) over the Indian low latitude sector. Adv. Space Res. 49 (5), 898–913.
Prölss, G.W., 1993. On explaining the local time variation of the ionospheric storm effects. Annals Geophys. 11 (1), 1–9.
Prölss, G., 1995. Ionospheric F-region storms. Handbook of atmospheric electrodynamics, edited by: Volland, H.
Radicella, S., Leitinger, R., 2001. The evolution of the DGR approach to model electron density profiles. Adv. Space Res. 27 (1), 35–40.
Rao, K., 2007. GAGAN-The Indian satellite based augmentation system. Indian J. Radio Space Phys. 36, 293–302.
Ratnam, D.V., Sarma, A., 2006. Modeling of Indian ionosphere using MMSE estimator for GAGAN applications. J. Ind. Geophys. Uni., 303–312
Sabzehee, F., Farzaneh, S., Sharifi, M.A., Akhoondzadeh, M., 2018. TEC Regional Modeling and prediction using ANN method and single frequency receiver over IRAN. Annals Geophys. 61 (1). https://doi.org/10.4401/ag-7297.
Scherliess, L., Fejer, B.G., 1999. Radar and satellite global equatorial F region vertical drift model. J. Geophys. Res.: Space Phys. 104 (A4), 6829–6842.
Seemala, G., Valladares, C., 2011. Statistics of total electron content depletions observed Over the South American Continent for the Year 2008. Radio Sci. 46. https://doi.org/10.1029/2011RS004722.
Sethi, N., Dabas, R., Sarkar, S., 2011. Validation of IRI-2007 against TEC observations during low solar activity over Indian sector. J. Atmos. Solar Terr. Phys. 73 (7–8), 751–759.
Sheela, K.G., Deepa, S., 2013. A new algorithm to find number of hidden neurons in Radial Basis Function Networks for wind speed prediction in renewable energy systems. J. Control Eng. Appl. Inform. 15 (3), 30–37.
Siddiqui, T.A., Lühr, H., Stolle, C., Park, J., 2015. Relation between stratospheric sudden warming and the lunar effect on the equatorial electrojet based on Huancayo recordings. Ann. Geophys. 33. https://doi.org/10.5194/angeo-33-235-2015.
Simpson, P.K., 1990. Artificial Neural Systems: Foundations, Paradigms, Applications, and Implementations. Pergamon.
Solomon, S.C., Qian, L., Burns, A.G., 2013. The anomalous ionosphere between solar cycles 23 and 24. J. Geophys. Res.: Space Phys. 118 (10), 6524–6535.
Song, R., Zhang, X., Zhou, C., Liu, J., He, J., 2018. Predicting TEC in China based on the neural networks optimized by genetic algorithm. Adv. Space Res. 62 (4), 745–759.
Stoneback, R., Heelis, R., Burrell, A., Coley, W., Fejer, B.G., Pacheco, E., 2011. Observations of quiet time vertical ion drift in the equatorial ionosphere during the solar minimum period of 2009. J. Geophys. Res.: Space Phys. 116 (A12).
Sugiura, M., Kamei, T., 1991. Equatorial Dst index 1957–1986. Int. Assoc. Geomagn. Aeronomy Bull. 40, 1–246.
Sur, D., Paul, A., 2013. Comparison of standard TEC models with a Neural Network based TEC model using multistation GPS TEC around the northern crest of Equatorial Ionization Anomaly in the Indian longitude sector during the low and moderate solar activity levels of the 24th solar cycle. Adv. Space Res. 52 (5), 810–820.
Takahashi, H., Costa, S., Otsuka, Y., Shiokawa, K., Monico, J., Paula, E., Nogueira, P., Denardini, C., Becker-Guedes, F., Wrasse, C., et al., 2014. Diagnostics of equatorial and low latitude ionosphere by TEC mapping over Brazil. Adv. Space Res. 54 (3), 385–394.
Tebabal, A., Radicella, S., Nigussie, M., Damtie, B., Nava, B., Yizengaw, E., 2018. Local TEC modelling and forecasting using neural networks. J. Atmos. Solar Terr. Phys. 172, 143–151.

Tshisaphungo, M., Habarulema, J.B., McKinnell, L.A., 2018. Modeling ionospheric foF2 response during geomagnetic storms using neural network and linear regression techniques. Adv. Space Res. 61 (12), 2891–2903.

Uwamahoro, J.C., Habarulema, J.B., 2015. Modelling total electron content during geomagnetic storm conditions using empirical orthogonal functions and neural networks. J. Geophys. Res.: Space Phys. 120 (12), 11000–11012. https://doi.org/10.1002/2015JA021961.

Uwamahoro, J.C., Habarulema, J.B., Okouma, P.M., 2018. Storm Time total electron content modeling over African low-latitude and midlatitude regions. J. Geophys. Res.: Space Phys. 123 (9), 7889–7905.

Uwamahoro, J.C., Habarulema, J.B., Buresova, D., 2019. Highlights about the performances of storm-time TEC modelling techniques for low/equatorial and mid-latitude locations. Adv. Space Res. 63 (10), 3102–3118.

Wanliss, J.A., Showalter, K.M., 2006. High-resolution global storm index: Dst versus SYM-H. J. Geophys. Res.: Space Phys. 111 (A2).

Williscroft, L.A., Poole, A.W., 1996. Neural networks, foF2, sunspot number and magnetic activity. Geophys. Res. Lett. 23 (24), 3659–3662.

Willmott, C.J., Matsuura, K., 2005. Advantages of the mean absolute error (MAE) over the root mean square error (RMSE) in assessing average model performance. Clim. Res. 30 (1), 79–82.

Yizengaw, E., Moldwin, M.B., Zesta, E., Biouele, C.M., Damtie, B., Mebrahtu, A., Rabiu, B., Valladares, C.F., Stoneback, R., 2014. The longitudinal variability of equatorial electrojet and vertical drift velocity in the African and American sectors. Annals Geophys. 32, 231–238.

Yonezawa, T., 1971. The solar-activity and latitudinal characteristics of the seasonal, non-seasonal and semi-annual variations in the peak electron densities of the F2-layer at noon and at midnight in middle and low latitudes. J. Atmos. Terr. Phys. 33 (6), 889–907.

Yuan, L., Soh, Y.C., Huang, G.B., 2010. Constructive hidden nodes selection of extreme learning machine for regression. Neurocomputing 73 (16–18), 3191–3199.